

Understanding Differences in the Crystallization Kinetics between One-Step Slot-Die Coating and Spin Coating of MAPbI₃ Using Multimodal In Situ Optical Spectroscopy

Konstantin Schötz, Christopher Greve, Arjan Langen, Harrie Gorter, Ilker Dogan, Yulia Galagan, Albert J. J. M. van Breemen, Gerwin H. Gelinck, Eva M. Herzig, and Fabian Panzer*

To develop a detailed understanding about halide perovskite processing from solution, the crystallization processes are investigated during spin coating and slot-die coating of MAPbI₃ at different evaporation rates by simultaneous in situ photoluminescence, light scattering, and absorption measurements. Based on the time evolution of the optical parameters it is found that for both processing methods initially solvent-complex-structures form, followed by perovskite crystallization. The latter proceeds in two stages for spin coating, while for slot-die coating only one perovskite crystallization phase occurs. For both processing methods, it is found that with increasing evaporation rates, the crystallization kinetics of the solvent-complex structure and the perovskite crystallization remain constant on a relative time scale, whereas the duration of the second perovskite crystallization in spin coating increases. This second perovskite crystallization appears restricted due to differences in solvent-complex phase morphologies from which the perovskite forms. The work emphasizes the importance of the exact precursor state properties on the perovskite formation. It further demonstrates that detailed analyses of multimodal optical in situ spectroscopy allows gaining a fundamental understanding of the crystallization processes that take place during solution processing of halide perovskites, independent from the specific processing method.


1. Introduction

Since the first reports on metal halide perovskites applied as absorber material in perovskite solar cells (PSCs), the efficiency of the latter has increased rapidly and is now at 25.5%.^[1–4] However, most highly efficient PSCs are processed on millimeter lab-scale dimensions using spin coating.^[5–11] To process perovskite layers from solution on a larger scale, methods such as slot-die coating are relevant. With slot-die coating, however, efficiencies of larger-scale PSCs are typically lower than their spin-coated counterparts.^[6,7,11] The main reason for this processing-dependent efficiency gap is seen in differences in the final layer properties that follow from the high complexity of the perovskite film evolution.^[8,11,12]

Thus, numerous works investigated the perovskite formation process using in situ characterization methods.^[6,13–18] Besides scattering techniques,^[19–24] also optical spectroscopy,^[25–28] with, e.g., absorption

K. Schötz, F. Panzer
Soft Matter Optoelectronics
University of Bayreuth
95440 Bayreuth, Germany
E-mail: fabian.panzer@uni-bayreuth.de

C. Greve, E. M. Herzig
Dynamics and Structure Formation - Herzig Group
University of Bayreuth
95440 Bayreuth, Germany

 The ORCID identification number(s) for the author(s) of this article can be found under <https://doi.org/10.1002/adom.202101161>.

© 2021 The Authors. Advanced Optical Materials published by Wiley-VCH GmbH. This is an open access article under the terms of the Creative Commons Attribution License, which permits use, distribution and reproduction in any medium, provided the original work is properly cited.

The copyright line for this article was changed on 1 September 2021 after original online publication.

A. Langen, A. J. J. M. van Breemen, G. H. Gelinck
TNO
Holst Centre
Eindhoven 5656 AE, Netherlands

A. Langen
TNO
Biobased and Circular Technologies
Auvergnedijk 2
Bergen op Zoom 4612 PZ, Netherlands

H. Gorter, I. Dogan, Y. Galagan
TNO

Partner of Solliance
Eindhoven 5656 AE, Netherlands

Y. Galagan
Department of Materials Science and Engineering
National Taiwan University
Taipei 10617, Taiwan

DOI: 10.1002/adom.202101161

and photoluminescence (PL) being measured in parallel during processing of halide perovskites from solution, or even combinations of scattering and optical spectroscopy,^[29,30] allowed to gain insights into the perovskite formation process.

Based on these studies, different structural dynamics, such as the formation of intermediate phases were observed during the early stages of solution processing, i.e., before the actual perovskite crystallization.^[31] In the case of coating the halide perovskite methylammonium lead iodide (MAPbI₃) from dimethylformamide (DMF) solution, the intermediate phase was associated with solvent-complex structures of the form (MA)₂(DMF)₂Pb₂I₆.^[32] These lead to needle-like structures in the final film,^[6,32] since the perovskite crystallization emanates from the complex structures retaining the needle-like morphology.

The needle-like solvent-complex morphology often results in an incomplete film coverage, detrimental for device efficiency.^[6] Thus in the past, strategies were developed to prevent the formation of needle structures during perovskite processing, realized by introducing additional processing steps, such as solution engineering approaches or heating steps.^[33–36] However, the implementation of such additional processing steps are often laborious to realize, especially in industry-relevant approaches such as role-to-role slot-die coating.^[37] Thus, ensuring a successful transfer of one-step solution processing of halide perovskites from spin coating to slot-die coating currently is a highly desired, yet not fully realized goal in the field.^[38]

To better control the crystallization processes and hence the subsequent film morphology across different processing methods, two aspects are crucial to address: First, we need to understand better how the crystallization of the solvent-complex structures is influenced by changes of the drying conditions, and secondly, how the subsequent perovskite crystallization kinetics are affected by differences in the solvent-complex structures.

In this work, we compare the crystallization kinetics that occurs during the processing of MAPbI₃ from DMF precursor solution via spin coating and slot-die coating. To change the crystallization kinetics, we systematically control the solvent drying conditions in both methods by changing the spin speed during spin coating and by changing the airflow above the wet film during slot-die coating using an air knife. To monitor the crystallization processes, we use multimodal in situ spectroscopy measuring in parallel absorption, PL, and light scattering during solvent-complex and subsequent perovskite formation. While absorption and PL give information on the formation of the perovskite, monitoring the evolution of scattered light enables quantifying the crystallization kinetics of optically inactive solvent-complex structures. This allows us to reveal that the crystallization mechanism of the complex structures appears to be independent of the processing method, whereas differences in the kinetics of the subsequent perovskite crystallization exist. In contrast to the case of slot-die coating, during spin coating we observe a second perovskite crystallization process, which is restricted due to higher polycrystallinity of the complex structures.

2. Results and Discussion

To monitor the optical properties in situ during MAPbI₃ processing from solution, we used the setup described by

Buchhorn et al.^[39] In brief, a white light LED is located below the substrate on which the perovskite precursor solution is processed. An optical fiber above the substrate detects the white light transmitted through the substrate and the material during processing. From this transmission spectrum, together with the transmission spectrum through a blank substrate (e.g., measured before the processing), the optical density (OD) is calculated.^[40] However, not only the absorption of the perovskite will contribute to the OD, but also the scattering of the white light at scattering centers in the investigated sample. To differentiate between the two effects, we use an additional LED, emitting at 2.5 eV (490 nm) placed above the substrate.^[39] This allows to better distinguish between absorption and scattering effects, as more scattering leads to an increase, while more absorption leads to a decrease of the detected scattering signal. In the following, we refer to this additional LED as “scatter-LED.” PL is excited with a laser placed above the substrate and detected by the same optical fiber. A detailed description of the setup and optical detection system can be found in Figure S1 in the Supporting Information.

2.1. Spin Coating of MAPbI₃

We processed MAPbI₃ thin films by one-step spin-coating a DMF precursor solution with a concentration of 0.7 M at eight different spin coating rotation speeds between 500 and 2000 rpm at ambient conditions (room temperature (RT), 50%–60% relative humidity). For example, **Figure 1** shows the evolution of PL, scatter-LED signal, and OD within the first 125 s of spin coating at 2000 rpm (see Figure S2, Supporting Information for other spin speeds). For the different optical properties, heat maps (bottom panel) together with spectra at selected times (top panel) after the start of spinning (corresponding to $t = 0$) are shown. While any PL is absent within the first 20 s (Figure 1a), a constant intensity of scattered LED light is present (Figure 1b), which we attribute to (time-invariant) light scattering at the chuck below the substrate and at the interfaces of substrate-solution and solution-air. Within this first time range, the OD spectra (Figure 1c) exhibit a wavelike modulation around zero intensity, where the periodicity of the modulation increases with spin coating time. This modulation is due to thin-film interference.^[40,41] From the periodicity of the modulation, together with the refractive index in which the interference occurs, the layer thickness can be calculated. By doing so, we find that the layer thickness of the solution drops to about 1 μm within the first 20 s of spin-coating (Figure S3, Supporting Information).

Up to 30 s no PL is observed (Figure 1a), whereas the detected intensity of the scatter-LED doubles within 5 s from 22 s onward (Figure 1b). Concomitantly, the OD at 1.55 eV increases from 0.0 to about 0.2, while the OD spectrum is nearly flat (Figure 1c). The increase in OD and I_{scatter} suggests the formation of structures at which the light from the white LED and the light from the scatter-LED are scattered. Due to the absence of any PL signature and absorption edge in the OD spectrum, we exclude the formation of MAPbI₃ to cause the increase in OD and I_{scatter} . Instead, we associate the appearance of the scattering centers with the formation of solvent-complex structures of the form (MA)₂(DMF)₂Pb₂I₆, as they were observed to occur

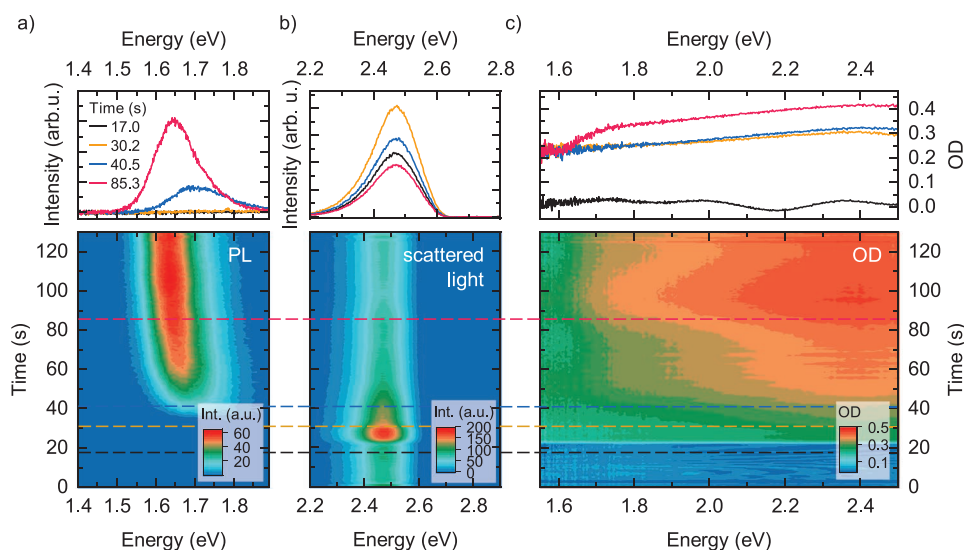


Figure 1. Spectra (top) and heat maps (bottom) of a) photoluminescence (PL), b) light scattering, and c) optical density (OD) measurement during the spin coating of a MAPbI₃ film at 2000 rpm.

during one-step processing of MAPbI₃ from DMF,^[6,32,40,42] and call the time of their onset $t_{0,\text{complex}}$. The light scattering from the solvent-complex structures results in a spectrally constant lift of the OD from $t_{0,\text{complex}}$ onward (Figure S4, Supporting Information), suggesting that at this stage, the solvent-complex structures already exhibit sizes larger than the wavelength λ of the scatter-LED, i.e., $>0.5\ \mu\text{m}$.^[43]

After 32 s, a broad, asymmetric PL peak appears at about 1.7 eV, where the high-energy edge is flatter than the low-energy edge (Figure 1a). The PL peak, which is associated with MAPbI₃ nuclei,^[40] then shifts quickly to lower energies and becomes narrower. Almost simultaneously to the rise of the MAPbI₃ PL, the detected intensity of the scattered LED light starts to decrease by about 30% of its maximum value within 5 s (Figure 1b), indicating the reduction of scattering species within the system. Between 30 and 40 s, the OD remains essentially unchanged except for a slight increase in OD intensity above $\approx 2.0\ \text{eV}$ (Figure 1c).

For $t > 40\ \text{s}$, the intensity of the PL increases, the peak width decreases, and the PL peak position shifts to lower energies, reaching $\approx 1.62\ \text{eV}$ at the end of the spin-coating process (Figure 1a). In this latter time range, the intensity of the scatter-LED signal continues to decrease, yet more slowly compared to the decrease between 30 and 35 s (Figure 1b). The PL increase and the decrease of the scatter-LED indicate a transition of complex phase to MAPbI₃.

In the OD spectra, the signature of the MAPbI₃ absorption edge appears in the form of an increase above 1.6 eV from about 40 s onward (Figure 1c).^[43,44] The absorption edge becomes more intense toward the end of spin coating. Above the MAPbI₃ absorption edge the OD is flat compared to the expected absorption coefficient of MAPbI₃,^[45] suggesting that the film is not fully covered by perovskites.^[43] In brief, a partial coverage of the substrate allows a certain fraction of the impinging light to pass the sample without being absorbed by the perovskite. Thus, a partial film coverage results in a certain minimum intensity of the transmitted light, which in turn sets an upper limit for the detectable OD. When approaching this

OD limit, the absorption spectrum becomes distorted and softly clipped (i.e., flatter),^[43] similar to an electrical signal in a triode tube gain stage upon grid-current clipping.^[46]

The observed changes of the optical spectra during spin coating are indicative of a nucleation and growth behavior. To access the crystallization kinetics of the complex phase and perovskite phase in a quantitative manner, it is necessary to extract the time evolution of different optical parameters, to analyze them in detail thereafter.

Before explaining which optical parameters we consider and how we extract them, we note that the evolution of the OD and the scatter-LED signal over time extracted from the raw data apparently exhibit a high degree of noise. Actually, the apparently high noise levels result from an aliasing effect due to the different frequencies of data acquisition and the rotating spin coater chuck. Filtering the corresponding beat frequency from the as-measured time traces significantly reduces the noise level (Figure S5, Supporting Information), and we only consider the filtered data for all further analysis.

To extract the time evolution of the PL peak position (Figure 2a, solid line), we fit an asymmetric hyperbolic secant to all detected perovskite PL spectra (see Figure S6, Supporting Information for details). The PL fitting approach also allows extracting the spectral positions where the PL has dropped to $1/e$ of the peak intensity on both sides of the peak-shaped PL spectrum. This spectral region is indicated as shaded area in Figure 2a, and with it, the evolution of peak asymmetry, as well as reduction of the peak width can be accessed. We extract the time evolution of the light scattering by considering the integrated intensity of the scatter-LED signal (referred to as I_{scatter}), shown in Figure 2b. Furthermore, we extract the evolution of the OD_{1.8eV} (Figure 2c), i.e., at a photon energy above the typical MAPbI₃ bandgap energy of $\approx 1.6\ \text{eV}$. Accordingly, the OD_{1.8eV} contains contributions from perovskite absorption and contributions due to the scattering effects within the sample. To extract the contribution from pure perovskite absorption, we calculate the difference between the OD at 1.8 eV and at 1.575 eV, i.e., $\Delta\text{OD} = \text{OD}_{1.8\text{eV}} - \text{OD}_{1.575\text{eV}}$ (Figure 2d). Here we

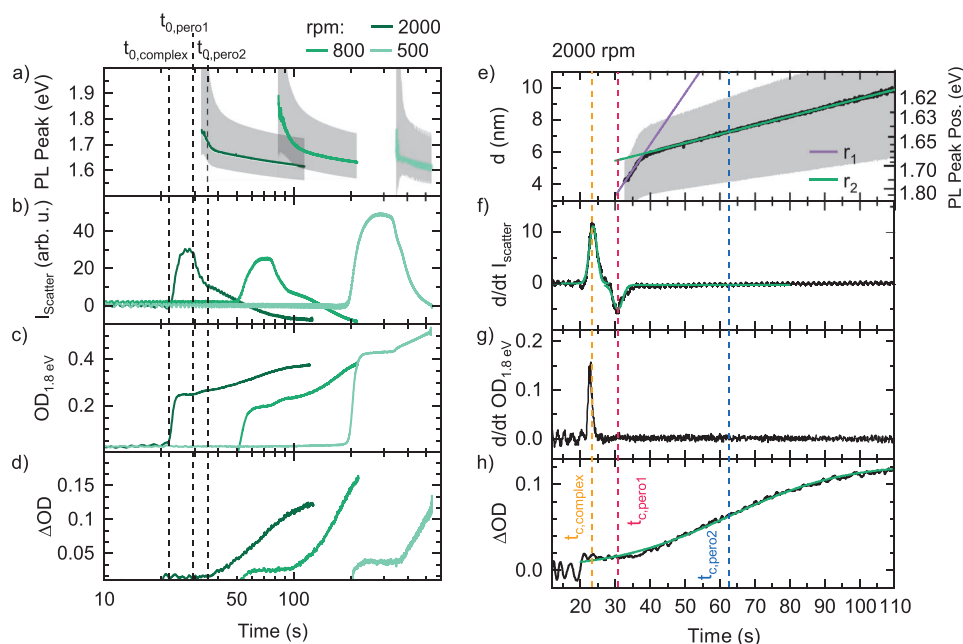


Figure 2. a–d) Time evolution of different optical parameters for spin coating with spin speeds of 2000 rpm (dark green), 800 rpm (green), and 500 rpm (light green). a) PL peak position, with the grey shaded area indicating the spectral range where the PL intensity is above $1/e$ of the peak intensity. b) Integrated intensity of the scatter-LED, I_{scatter} . c) OD at 1.8 eV. d) ΔOD , i.e., the difference of the OD at 1.8 and at 1.575 eV. Vertical dashed lines indicate the onsets t_0 of the different crystallization processes for a spin speed of 2000 rpm. e–h) Analyses of the optical parameters for spin coating at 2000 rpm. e) Average crystallite size determined from the PL peak position using Equation (1). The shaded area indicates the sizes depending on the value of parameter b in Equation (1). f) The derivative of I_{scatter} . g) The derivative of OD_{1.8eV} and h) ΔOD together with fits (green lines) as described in the main text. Dashed vertical lines indicate the critical times t_c of the different crystallization processes.

assume that an increase in OD_{1.575eV}, i.e., at energy below the MAPbI₃ bandgap, is caused exclusively by light scattering. This approach is a valid approximation to the absorption of the perovskite only since the scattering contribution in the OD is only weakly energy dependent. Additionally, the influence of this energy dependence on the ΔOD is minimized by choosing the OD at energies which are close to each other.

From Figure 2a–d it becomes clear that for all spin speeds the different optical parameters proceed in the same qualitative fashion as a function of spin coating time, though they are slower for decreasing spin speeds.

Next, we want to gain a more detailed understanding of the various crystallization processes occurring during spin coating, based on a detailed examination of the evolution of the optical parameters with time. This will be carried out in the following as an example for the case of 2000 rpm.

As already discussed in Figure 1, the formation of solvent-complex phase is reflected in the initial increase of OD_{1.8eV} and I_{scatter} starting from $t_{0,\text{complex}}$. After the initial increase, both signals saturate, followed by a rapid decrease of I_{scatter} onward. This point in time we refer to as $t_{0,\text{pero1}}$. A decrease of I_{scatter} can either result from a reduction of scattering structures or result from increasing absorption at the wavelength of the scatter-LED. The fact that OD_{1.8eV} increases during the decrease of I_{scatter} , speaks against a reduction in scattering structures. Rather, e.g., after 40.5 s, OD spectra exhibit a slight increase toward higher photon energies, in contrast to the flat OD spectra before $t_{0,\text{pero1}}$ (e.g., $t = 30.2$ s). This additional contribution to the OD spectra could stem from Rayleigh scattering at

structures significantly smaller than the wavelength range of the white light, as it would be the case for perovskite nuclei. The initial perovskite nuclei are likely to exhibit a quantum confinement effect, shifting the corresponding bandgap to higher (e.g., > 1.8 eV) energies.^[47] Hence ΔOD calculated based on OD_{1.8eV} might not capture the appearance of absorption from perovskite nuclei that only absorb at higher energies due to a quantum confinement effect. Considering the temporal evolution of ΔOD calculated based on OD_{2.2eV} (Figure S7, Supporting Information), indeed shows an increase after $t_{0,\text{pero1}}$, which is similar to the corresponding increase in OD_{1.8eV}. Thus, we associate the decrease in I_{scatter} to stem from an increase in absorption due to the formation of nanosized perovskite crystals.

A formation of nanosized perovskite crystals is further supported by the fact that the first perovskite PL that could be detected shortly after $t_{0,\text{pero1}}$ is at higher photon energies and exhibits a flatter high-energy edge, compared to bulk PL spectra of MAPbI₃ (Figure S8, Supporting Information). The broadened PL in combination with the PL shift indicates that the PL exhibits a quantum confinement effect due to a perovskite crystal size below the corresponding quantum confinement limit, which was found to be 20–30 nm for MAPbI₃.^[47–51] This is also in line with the formation of first nanosized perovskite crystals starting from $t_{0,\text{pero1}}$.

Finally, the beginning of a second perovskite formation process is indicated by the significant increase in ΔOD , the slower shift of PL peak position to lower photon energies, and the slowing down of the decrease of I_{scatter} all starting from

t_{0, pero_2} . Thus, independent from the spin speed, we observe the crystallization processes occurring during spin coating to proceed in the order i) formation of solvent-complexes (in the following referred to as “solvent-complex phase”), ii) formation of nanoconfined perovskite grains (“pero₁ phase”), iii) second perovskite formation process (“pero₂ phase”).

As a next step, we analyze the decrease of the PL peak position (Figure 2a) in more detail. The perovskite PL exhibits a nanoconfinement effect. In such a case, based on quantum mechanical considerations, it was suggested that the PL peak position E_{PL} depends on the average crystallite size d by

$$E_{\text{PL}}(d) = E_g + b/d^2 \quad (1)$$

where E_g is the bulk PL position and b is a constant.^[52] We use Equation (1) and calculate the evolution of the average MAPbI₃ crystal size for the different spin speeds over time based on the PL peak positions from Figure 2a. Since the parameter b is reported to be in the range of 1–5 eV nm² for MAPbI₃,^[51,53] we use an average value of 3 eV nm² and $E_g = 1.59$ eV (Figure S8, Supporting Information). Figure 2e exemplarily shows the time evolution of the average crystal size calculated this way for spin coating at 2000 rpm. We consider the average crystal sizes that result when using 1 and 5 eV nm² in Equation (1) as upper and lower error limits, respectively. The resulting error range of average crystal sizes is indicated as the grey shaded area. After about 32 s, the average perovskite crystal size d increases fast from 4 to 6 nm within 6 s and then increases more slowly, reaching 10 nm after 110 s. Using linear fits in the time range of the fast (purple solid line) and slow increase (green solid line) of d allows extraction of perovskite crystal growth rates of 0.32 and 0.06 nm s^{−1}, respectively.

To interpret the average crystallite sizes and thus the growth rates in a substantiated manner, one must also consider that in general, the strongest contribution to the overall confinement effect stems from the shortest length within a crystal.^[51] This means that in crystal structures where only one length is below the confinement limit, a quantum confinement effect still occurs.^[51] Thus the growth of perovskite crystal size during the pero₂ phase is not necessarily inhibited in all spatial directions, but at least in one.

In general, self-absorption effects can have a significant influence on the PL properties,^[40,54–58] where the PL peak is shifted to lower energies and/or even additional PL features at lower energies compared to the intrinsic PL can appear.^[40,54–57] If self-absorption was significant in our data, its impact would become more significant with time, as more perovskite phase is present in the sample. With time, the average crystal size calculated according to Equation (1) would more and more overestimate the actual crystal size and thus the corresponding extracted growth rate. However, since in Figure 2a, the PL peak position is always at significantly higher energies than the bulk PL of MAPbI₃, self-absorption appears to be negligible in our data.

In Figure 2a–d we identified the onset-times of the solvent-complex phase, pero₁ phase, and pero₂ phase. To quantify the kinetics of the different crystallization processes in more detail, we analyze the time evolution of the optical parameters shown in Figure 2b–d.

We follow an analysis approach that we used previously to determine the kinetics of the recrystallization process of MAPbI₃ during solution-based two-step processing.^[40] To this end, we calculate the derivative of I_{scatter} and OD_{1.8 eV} with time from Figure 2b,c. This results in peaks that occur at the times of the different crystallization processes in the corresponding dI_{scatter}/dt and dOD/dt diagrams. Using Gaussians, we fit these peaks and associate the time of a peak maximum with the critical time t_c , and the width $w = 2\sigma$ with the duration of the individual crystallization processes.

This analysis procedure is exemplified in Figure 2f,g for the measurement at 2000 rpm. Due to the clear peak signatures of the solvent-complex formation process in both dI_{scatter}/dt (Figure 2f) and dOD/dt (Figure 2g), we can extract $t_{c, \text{complex}} = 23.2 \pm 0.4$ s and width $w_{\text{complex}} = 1.7 \pm 0.6$ s. The steep decrease of I_{scatter} observed from t_{0, pero_1} onward in Figure 2b, manifests itself as a peak to negative values at t_{c, pero_1} in Figure 2f. This peak is significantly more intense than the corresponding feature of the pero₁ phase in the dOD/dt graph (Figure 2g). Thus a reliable quantification of both $t_{c, \text{pero}_1} = 30.9$ s and the corresponding $w_{\text{pero}_1} = 3.1$ s is possible from dI_{scatter}/dt . However, in both dI_{scatter}/dt and dOD/dt , the noise level obscured any signature of the pero₂ formation phase. To not worsen the signal-to-noise-level by calculating $dOD_{1.8 \text{ eV}}/dt$, we analyze the evolution of ΔOD directly by fitting the error function (that is, the integral of the Gaussian function used above) to the transition (Figure 2h). This allowed to quantify the pero₂ formation process satisfyingly, where we obtain $t_{c, \text{pero}_2} = 62.7$ s and $w_{\text{pero}_2} = 52.2$ s. Overall, it is possible to quantify the critical times t_c and corresponding temporal durations of all three crystallization processes (solvent-complex formation, pero₁ phase and pero₂ phase formation) that appear during spin coating.

The different t_c and widths for the different crystallization processes are shown in Figure 3a as a function of the spin speed. Here, the time sequence of film formation is represented in a columnar form, and the time ranges in which the different

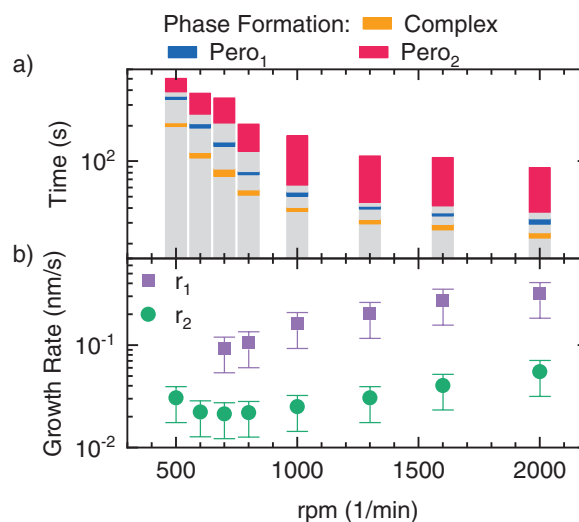


Figure 3. a) Color bar representation of the critical times t_c and widths of the different crystallization phases. b) Perovskite growth rates extracted from the evolution of average crystal size during spin coating (see Figure 2e for 2000 rpm), as a function of spin speed.

crystallization processes occur are colored. The temporal position and width of the colored areas correspond to the t_c and the width w , i.e., each colored area covers the time range $t_c \pm w$ (see also Figure S9 in the Supporting Information for a separated representation of t_c and w). As expected, t_c and corresponding width of all crystallization processes decrease with increasing spin speed due to the accelerated solvent evaporation, i.e., all crystallization processes occur earlier and faster with increasing rpm (also see Figure S9, Supporting Information). It is also evident from Figure 3a that the time duration of the perov_2 formation relative to the time durations for the complex phase and perov_1 -phase tend to increase with spin speed.

Figure 3b shows the perovskite growth rates extracted following the analysis approach from Figure 2e, as a function of spin speed, where the growth rates at early times (r_1) are about an order of magnitude higher than the growth rates at later times (r_2), with both rates increasing for increasing rpm.

Thus, so far, we could establish all analytical approaches to identify and quantify the different crystallization processes occurring during spin coating. Next, we use these analytical approaches to also investigate the crystallization processes that take place during slot-die coating.

2.2. Slot-Die Coating of MAPbI₃

We processed MAPbI₃ thin films by slot-die coating, using the same precursor solution and ambient conditions as for spin coating, and monitored the film formation by in situ optical spectroscopy. Due to technical reasons, the scatter-LED implementation, as used in the spin coating measurements, was not feasible in the slot-die coater. To still be able to monitor the scattering of solvent-complexes during the processing, we exploit the ambient room light that was available during all slot-die coatings and measured its scattered intensity. However, in contrast to the scatter-LED, the room light is also present during

the OD measurement. Consequently, the background correction recorded before the coating loses its validity upon the formation of scattering centers during slot-die coating. This can lead to distinct spectral features of the room light appearing in the OD spectra. Nevertheless, because of the distinct spectral signatures of the room light, it can be easily distinguished from the optical signatures of solvent-complexes and MAPbI₃.

To control the crystallization kinetics during slot-die coating we use an air knife, mounted just above the carrier parallel to the substrate. With increasing air pressures from 0.5 to 4 bar through the air knife, solvent evaporation can be increased (see Figure S1, Supporting Information for technical details).

Figure 4 shows the evolution of optical properties measured during slot-die coating using an air pressure of 4 bar (see Figure S10, Supporting Information for other air pressures). Analogous to Figure 1, Figure 4 shows the PL, the scattered room light, and the OD as a heat map (bottom panel), together with individual spectra at selected times (top panel). The time axis was chosen so that $t = 0$ coincides with the moment the slot-die head reaches its final position after dispensing the precursor solution on the substrate, which is ≈ 1.5 s (see the Supporting Information for technical details).

Within the first 70 s of slot-die coating, no optical signatures of both perovskite and complex structures were observed and no periodic modulation in the OD spectra was present. A lack of modulation in the OD spectra suggests that the height of the solvent layer that could cause an interference effect is larger than the coherence length of the detected light ($\approx \mu\text{m}$ range). The corresponding analysis in the case of spin coating suggested that the first spectral modulations were linked to a highest detectable layer thickness in the range of $\approx 10 \mu\text{m}$ (Figure S3, Supporting Information). As we used the same white LED also in the slot-die coating experiments, the absence of modulations in the OD spectra in Figure 4c suggests that the solvent level at the moment of the initial complex phase formation was at least $\approx 10 \mu\text{m}$.

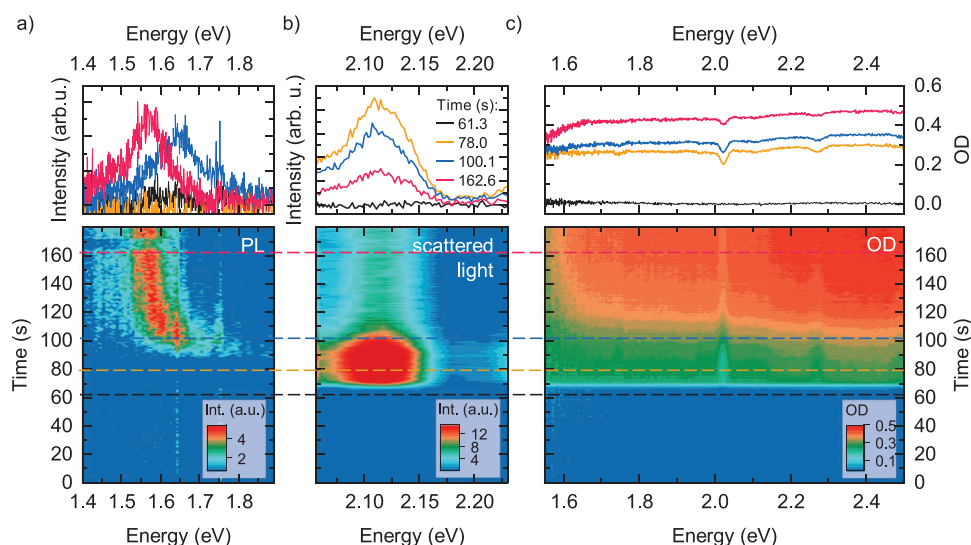


Figure 4. Spectra (top) and heat maps (bottom) of a) photoluminescence (PL), b) light scattering, and c) optical density (OD) during the slot-die coating of a MAPbI₃ film at an air knife pressure of 4 bar. The drop of the PL between 160 and 170 s is due to a fluctuation of the power of the excitation laser.

In the time range from 70 to 90 s, the optical signatures of growing solvent-complex structures become apparent, with the intensity of the scattered light increasing significantly, while concomitantly, the OD increases almost independent from the photon energy. As expected (vide supra), the increase in scattered room light leads to distinct features (e.g., near 2.0 eV) in the OD spectra, while no OD or PL signatures of MAPbI₃ are yet detectable.

After 90 s a PL peak at 1.7 eV appears, which shifts to lower energies for longer times, reaching a final PL peak position of 1.59 eV after 160 s. This final PL peak position matches the PL peak position of bulk MAPbI₃. Compared to the spin coating case the PL intensity is lower, which we associate with a reduced sensitivity for light detection of the measurement setup when implemented at the slot-die coating setup. Simultaneous to the appearance of PL signal, the intensity of the scattered light decreases, reaching a constant intensity after about 120 s, indicating the transition from complex to perovskite phase as was also seen in the spin coating case. Starting from about 100 s, the OD increases more steeply, and concomitantly, an absorption edge of MAPbI₃ at 1.65 eV becomes apparent (see OD at $t = 100$ s), gaining intensity at later times (see OD at $t = 162.6$ s). As in the case of spin coating, the flat shape of the OD above the absorption edge indicates incomplete substrate coverage also in the case of slot-die coating.^[43]

Analogous to the procedure in Figure 3, we extract the evolution of different optical parameters over time for all measured air knife pressures, which is shown for PL peak position and OD at 1.8 eV in **Figure 5** (see Figure S11, Supporting Information for the evolution of ΔOD and I_{scatter}). The PL peak position was determined in the same way as in Figure 2a. For the sake of clarity, the decay to $1/e$ is not indicated here (see Figure S12, Supporting Information for a more detailed version of Figure 5a).

For all air knife pressures, the PL peak shifts from 1.7 to 1.59 eV and saturates thereafter (Figure 5a). As in the case of spin coating, we interpret the appearance of a PL signal shifted to higher energies than typically observed for the corresponding bulk value as the signature of perovskite nuclei exhibiting a quantum confinement effect. These nuclei grow continuously

in size, indicated by the shift of the PL peak position to lower energies. The saturation of the PL peak position at the energy of the bulk MAPbI₃ PL (Figure S8, Supporting Information), which occurs for all air pressures used here, suggests that the perovskite crystallites grow to sizes larger than the length scale of the confinement limit (20–30 nm).^[51]

The time evolution of OD_{1.8 eV} exhibits a two-step increase for all air knife pressures (Figure 5b). Further considering the signatures in the evolution of I_{scatter} and ΔOD (Figure S11, Supporting Information), we associate the first OD increase with the formation of complex phase and the second increase with the formation of perovskites. Thus, in contrast to the spin coating, for slot-die coating only one perovskite crystallization process occurs.

We extract t_c and corresponding widths based on the evolution of the optical parameters from Figure 5a,b and Figure S11 in the Supporting Information, analogously to the analysis methods used in Figure 2f–h. Figure 5c shows t_c and widths of the complex (orange) and perovskite formation (blue) on a logarithmic time scale, in the same way the times and durations of the crystallization process occurring during spin coating were presented in Figure 3a (see Figure S13, Supporting Information for alternative version). As expected, as solvent evaporation accelerates with increasing air knife pressures, complex and perovskite formation occur at earlier times and their time widths are reduced. No significant increase in the width of perovskite phase formation relative to the width of complex phase formation seems to occur in Figure 5c for increasing evaporation rate (i.e., for increasing air knife pressures). This constant relative width of perovskite crystallization is reminiscent to the evolution of the pero_1 width, but clearly contrasts the corresponding relative widths for the pero_2 phase in the case of spin coating (Figure 3a).

Analogously to Figure 2e, we estimate the evolution of average perovskite crystallite sizes from the evolution of the PL peak position over time. From the time-dependent increase of the perovskite crystal size, we extract the growth rate of the perovskite crystallites (see Figure S14, Supporting Information), which is plotted as a function of air pressure in Figure 5d. We find the growth rate to increase with air knife pressure,

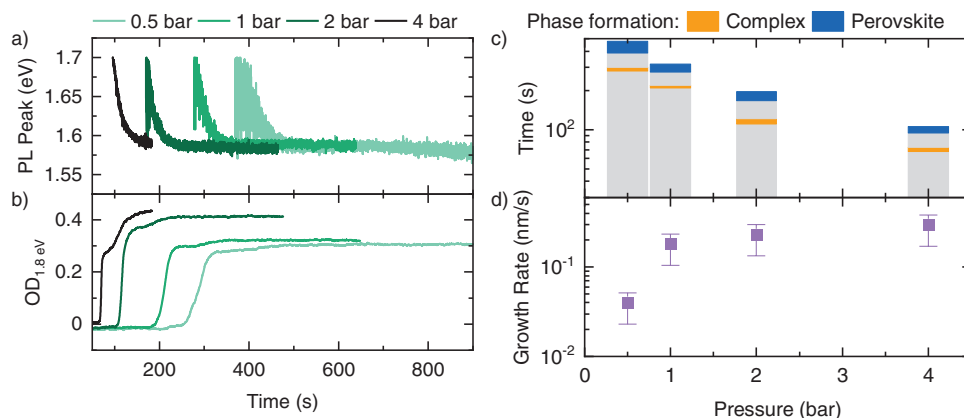


Figure 5. a) PL peak position and b) OD_{1.8 eV} for slot-die coating with different air pressures at the air knife. c) Critical times t_c and widths w of the complex (orange) and perovskite (blue) phase formations and d) perovskite growth rate as extracted from the PL peak position using Equation (1) as a function of the air pressure at the air knife.

exhibiting values in a similar range as those extracted during the early perovskite crystallization for spin coating (compare r_1). We note that since the PL peak position saturates at the value of bulk MAPbI₃ for all air pressures, we conclude that self-absorption again has a negligible or only minor effect on the PL peak position in our measurements.

In summary, analogously to the analysis for spin coating, the different crystallization processes during slot-die coating were quantified and the findings of the spin coating were used to identify qualitative differences and similarities in the crystallization behavior between spin and slot-die coating. In the following, we aim for a systematic and quantitative comparison of the crystallization processes of the two processing methods.

2.3. Comparison of Spin- and Slot-Die Coating

If the crystallization mechanisms do not change, a higher evaporation rate would only result in a corresponding decrease of the crystallization durations and a corresponding reduction of their time differences. Accordingly, one would expect that with suitable normalization, the relative crystallization durations should be independent of the evaporation rate.

We thus aim for considering the durations of the various crystallization processes identified in Figures 3a and 5c relative to each other. We first consider the slot-die coating process, and by using the widths and times of the crystallization processes obtained in Figure 5c, we normalize to the time difference $\Delta t_c = t_{c, \text{pero}} - t_{c, \text{complex}}$. To do this, we subtract the time $t_{c, \text{complex}}$ from all different times, so that $t_{c, \text{complex}}$ always is 0. Then we

divide all times (t_c and widths) by the absolute value of Δt_c , so that after normalization $t_{c, \text{pero}}$ is 1 (Figure 6a).

From a zoomed-in version of Figure 6a, it becomes clear that the widths of the complex formation and perovskite formation are nearly independent of the air knife pressure (Figure 6b). This supports the hypothesis that an increase of the air knife pressure leads to an acceleration of the film formation, but the mechanisms of the crystallization processes do not change in the case of slot-die coating.

In analogy to Figure 6a, we normalize the t_c and widths of the spin-coating crystallization processes from Figure 3a for all investigated spin speeds (Figure 6c). For the normalization we consider the pero_1 formation, i.e., t_{c, pero_1} and corresponding time duration (see Figure S15, Supporting Information for a version normalized to t_{c, pero_2}). In Figure 6c, the pero_2 formation takes a large fraction of the overall film formation time on this relative time scale, with the width and critical time of the pero_2 formation increasing with increasing spin speed. In contrast, the relative widths of the solvent-complex phase (orange) and the pero_1 phase (blue) are largely independent of spin speed (Figure 6d). Furthermore, the relative widths of complex formation and pero_1 formation for spin coating and slot-die coating are similar (Figure 6c,d). This suggests that the crystallization mechanisms of solvent-complexes and the subsequent perovskite crystallization are comparable in both processing methods, whereas the crystallization of the pero_2 crystallization phase in spin coating differs from the other perovskite crystallization processes.

The independence of the formation mechanism of the solvent-complex structures from the processing method suggests that $t_{c, \text{complex}}$ or width w_{complex} are most suitable as independent

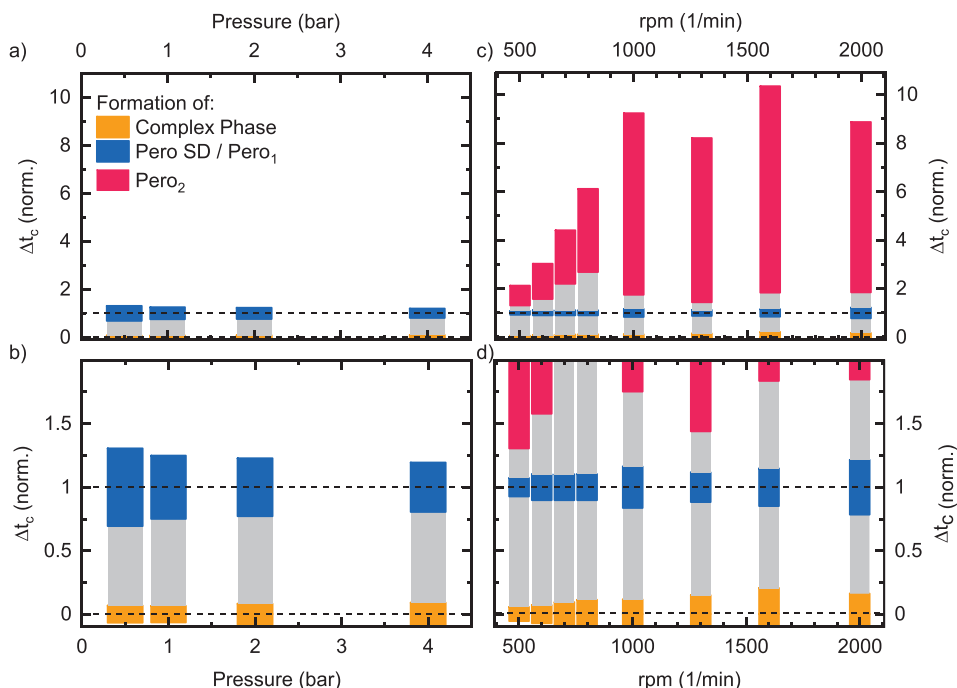


Figure 6. Bar chart of critical time t_c and widths w of the phase formations upon slot-die coating a,b) and spin coating c,d), normalized to $\Delta t_c = t_{c, \text{pero}} - t_{c, \text{inter}}$, i.e., $t_{c, \text{inter}}$ is 0 and $t_{c, \text{pero}}$ is 1. b,d) Zoom-in versions of (a,b).

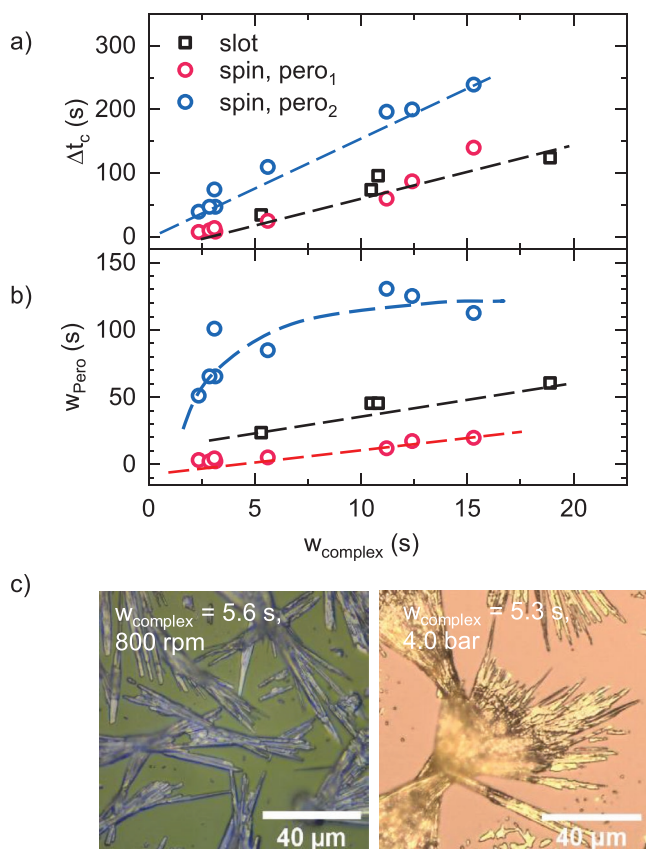


Figure 7. a) $\Delta t_c = t_{c,\text{perov}} - t_{c,\text{complex}}$ and b) width of the perovskite formation w_{perov} as a function of the width of the complex phase formation w_{complex} for slot-die coating (black squares) and first (pero_1 , red circles) and second (pero_2 , blue circles) perovskite crystallization during spin coating. c) Microscopy images of spin coated (left panel) and slot-die coated (right panel) thin films with comparable w_{complex} (for complete list of microscopy images see Figure S17 in the Supporting Information).

parameters to systematically compare the perovskite formation kinetics between spin coating and slot-die coating. As the time zero is often difficult to determine precisely and thus also $t_{c,\text{complex}}$ is, we use w_{complex} as a common parameter and plot both $\Delta t_c = t_{c,\text{perov}} - t_{c,\text{complex}}$ and w_{perov} as a function of w_{complex} for the different perovskite crystallization phases (Figure 7).

In general, Δt_c increases linearly with increasing w_{complex} (i.e., with decreasing air pressure or spin speed), with the values for slot-die coating ($\Delta t_{c,\text{slot}}$, black squares) and for the first perovskite crystallization in spin coating ($\Delta t_{c,\text{pero1}}$, red circles) exhibit virtually the same increase (Figure 7a). This further indicates that the mechanism of these two perovskite crystallization processes is similar. In contrast, the value for the pero_2 crystallization ($\Delta t_{c,\text{pero2}}$, blue circles) increases more steeply, i.e., for a certain w_{complex} the pero_2 crystallization in spin coating occurs considerably delayed compared to the perovskite formation in slot-die coating. The different slopes between $\Delta t_{c,\text{pero2}}$ in spin coating and $\Delta t_{c,\text{slot}}$ (and $\Delta t_{c,\text{pero1}}$ respectively), suggest that the mechanism of the pero_2 crystallization in spin coating differs from the corresponding mechanism of the one in slot-die coating (and from the first perovskite crystallization in spin coating respectively).

This difference in crystallization behavior is also reflected in the dependence between w_{perov} and w_{complex} (Figure 7b). Here w_{perov} of the slot-die coating and $w_{\text{pero1,spin}}$ of the spin coating increase linearly with w_{complex} , exhibiting almost identical slopes. In contrast, $w_{\text{pero2,spin}}$ exhibits a non-linear dependence, with a steep increase followed by a flattening out for larger w_{complex} , always at values higher than $w_{\text{pero1,spin}}$ and $w_{\text{perov,slot}}$.

Plotting the perovskite growth rates extracted from the PL peak shifts as a function of width w_{complex} , shows that the rates associated with pero_1 during the spin coating are similar to those associated with the perovskite growth during slot-die coating, and both decrease similarly with increasing w_{complex} (Figure S16, Supporting Information). In contrast, the growth rate occurring during the pero_2 formation is significantly diminished by about one order of magnitude. This is in line with the assumption that the mechanism of perovskite crystallization during slot-die coating and the pero_1 crystallization in spin coating is similar, while the pero_2 crystallization in spin coating is more restricted.

To understand the impact of the different crystallization mechanisms on the final film morphology, we took microscopy images of the films processed by spin coating and slot-die coating, where in Figure 7d films with similar w_{complex} are shown. This, for example, was the case for a spin speed of 800 rpm ($w_{\text{complex}} = 5.6$ s) and an air knife pressure of 4 bar ($w_{\text{complex}} = 5.3$ s). As expected, both films show a needle-like morphology determined by the complex structures with an incomplete film coverage. For both processing methods, it can be observed that the film coverage becomes more homogeneous, and the needle structures become smaller with faster drying kinetics (Figure S17, Supporting Information). In general, the needles are arranged in bundles, with a certain preferential direction. However, the degree of orientation of the bundles seems to be somewhat less pronounced in the slot-die coated film than in the spin-coated film. The dark areas inside the needles in both films correspond to perovskite phase,^[59] suggesting that the latter forms within the solvent-complex structures.

Furthermore, in the slot-die coated film, the yellow out-of-focus areas demonstrate that the needles in the center of the bundle are not in the focal plane of the microscope. This suggests that in the center of the bundles, needles grew also into vertical direction. For the film processed by spin coating, growth of the needles out of the focus plane can only be observed, at higher magnification (i.e., smaller focus depth), for the slower spin speeds (Figure S17, Supporting Information). Furthermore, profilometry measurements of the different spin coated films show that with increasing rpm, the mean height of the thin film decreases (Table S1, Supporting Information). In summary, these results suggest that the needle morphology in spin coating is flatter than in slot-die coating.

Thus, despite similar complex phase formation dynamics, the final film morphology between slot-die coated and spin coated films clearly differs. Since the perovskite phase forms and grows within the needles of the complex phase, it stands to reason that differences in solvent-complex phase morphology are responsible for the differences in perovskite growth between spin and slot-die coating.

2.4. Discussion

Based on the previous results, all the necessary knowledge could be derived to develop a complete picture of the differences in crystallization processes during spin- and slot-die coating, which will be discussed in the following. The sequence of crystallization processes, normalized to the duration of complex phase formation, analogously to the procedure in Figure 7, is illustrated in **Figure 8**.

As inferred from the temporal increase of I_{scatter} and OD, in both processing methods needle-like solvent-complex structures crystallize first (Figure 8a).^[32]

Independent from the specific solution processing method, the formation process of the complex phase follows from a supersaturation-induced heterogeneous nucleation and growth process, as suggested by Fong et al.^[14] Upon their first detection, i.e., from $t_{0,\text{complex}}$ onward, the needles are already μm -sized, as suggested by the scattering contribution of the solvent-complex structures being independent of photon energy. For both processing methods the size of the needles increases to above $\approx 50 \mu\text{m}$ in the final film (Figure S17, Supporting Information).

However, in spin coating, the white light interference in the OD spectra at the beginning of the processing revealed that at the time of the first detection of the complex structures, the solvent level had already dropped to a few μm . Accordingly, in the case of spin coating, we conclude that the growth of needles perpendicular to the substrate is limited by the decreasing solvent level from a certain point during spin coating. Further, for increasing rpm we observed that the solvent level just before $t_{0,\text{complex}}$ decreases (Figure S3c, Supporting Information), while at the same time the complex phase formation accelerates (decreasing w_{complex} Figure 3b; Figure S9, Supporting Information). This indicates that for increasing rpm, the decreasing solvent level influences the growth of the complex phase needles over a longer relative time span. As it is possible to explain the flat needle morphology to be the result of the decreasing solvent levels, shear forces in the needles, induced by centrifugal forces during substrate rotation, might not alter the needle growth direction significantly in case of spin coating.

In contrast, in slot-die coating the solvent level just before $t_{0,\text{complex}}$ could be estimated to be at least $10 \mu\text{m}$. This might suggest that the complex phase formation during slot-die coating is not significantly limited by the solvent level (Figure 8b). This fits with the needle structures observed in Figure 7, some of which protrude considerably upward in the slot-die coated sample, whereas a flat needle morphology is present in the spin-coated sample.

After the complex structure formation, the perovskite crystallizes within the complex structures (Figure 8c), which could be inferred from the time evolution of the optical parameters and from the microscopy images (Figure S17, Supporting Information). Examining the formation kinetics of $\text{pero}_{\text{slot}}$ and $\text{pero}_{1,\text{spin}}$, similar growth rates (Figure S16, Supporting Information) and Δt_c values (Figure 7a) for comparable w_{complex} (Figure 7a) indicate that their crystallization behavior is similar (Figure 8d).

However, in contrast to slot-die coating, a significant reduction of the perovskite growth rate in at least one spatial direction occurs in spin coating after exceeding an average crystal

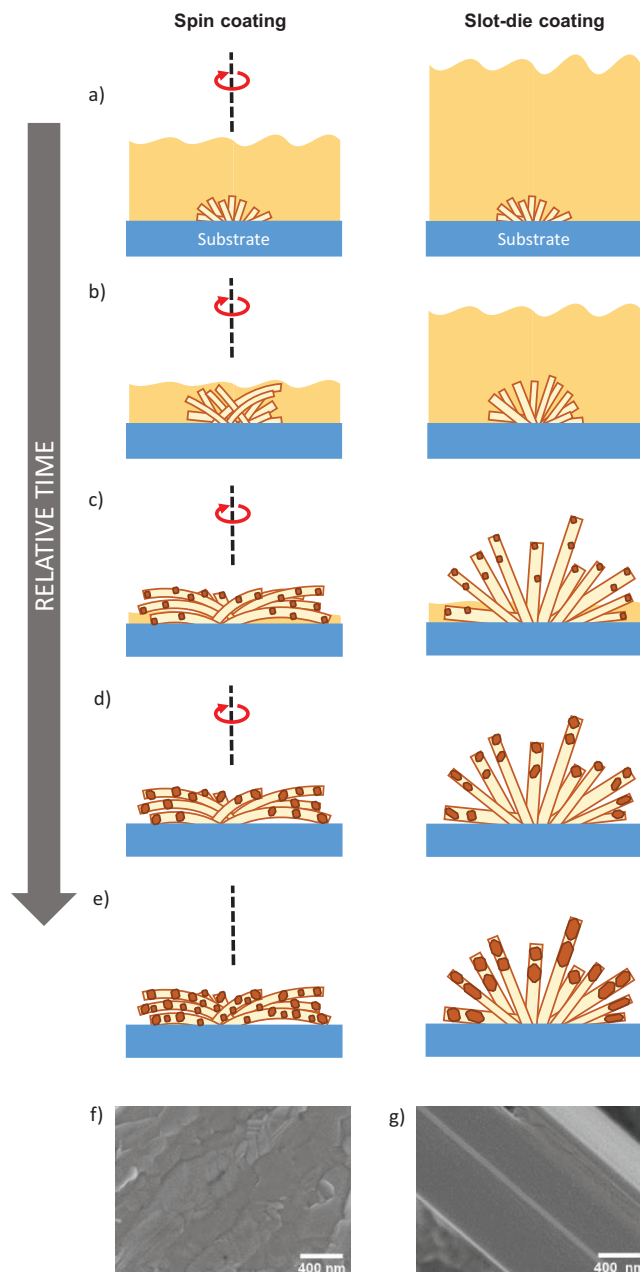


Figure 8. a–e) Illustration of the crystallization processes occurring during spin- (left) and slot-die coating (right) on a relative time axis, which is normalized to the duration of the complex phase formation. Supersaturated precursor solution leading to the initial solvent-complex phase nucleation is depicted in orange, while solvent-complexes are in beige and perovskite nuclei in brown. f, g) SEM images of a spin-coated MAPbI₃ thin film f) and a film obtained by drop casting g). For full list of SEM images see Figure S18 in the Supporting Information.

size of about 5–7 nm (Figure 2e). This suggests a restricted crystallization for $\text{pero}_{2,\text{spin}}$ compared to $\text{pero}_{\text{slot}}$ and $\text{pero}_{1,\text{spin}}$. In addition to the reduced growth rate, the second perovskite formation process during spin coating proceeded over a longer relative time span than the first perovskite formation phase, an effect that intensified with increasing spin speed (Figure 7b). These results suggest that the changed crystallization properties

of $\text{per}_{0.2,\text{spin}}$ are related to the flattened needle-like morphology of the complex phase. The growth rates we observe (Figure S16, Supporting Information) are significantly lower compared to values reported for other synthesis approaches where the perovskite forms directly, ranging from about 10 nm s^{-1} to $1 \mu\text{m s}^{-1}$.^[40,60–62] This indicates that perovskite formation from a solvent-complex phase is considerably slower than direct perovskite phase formation from solution. Accordingly, it is reasonable to assume that the morphology of the complex phase has a significant influence on the perovskite crystallization. Hence this further supports that the altered crystallization properties of $\text{per}_{0.2,\text{spin}}$ could be the result of a changed morphology of the complex phase.

A possible reason for the restricted perovskite crystallization could be an increased polycrystallinity of the solvent-complex structures. We speculate that an increased bending of the needle during growth, or growth along a non-preferred orientation parallel to the solvent surface could lead to more deficient growth and thus increased polycrystallinity in the complex needle. Consequently, the growth of perovskite nuclei would be restricted when reaching a solvent-complex phase grain boundary, resulting in overall smaller perovskite crystallites. In the wake of less restricted solvent-complex growth, as it appears to be the case for slot-die coating, the perovskite phase can crystallize more unhindered.

A more unhindered perovskite crystallization for slot-die coating is in line with our observations of the perovskite crystal size exceeding the confinement limit (Figure 8e). Furthermore, scanning electron microscopy (SEM) images of the final morphologies demonstrate that in the spin coating case (Figure 8f), the needle morphology is determined by many small grains. In contrast, the needle structures resulting from slot-die coating (Figure 8g) appear significantly less polycrystalline, with grain sizes $>1 \mu\text{m}$.

Thus, it becomes clear that based on the knowledge gained from the detailed analyses applied to the multimodal optical in situ spectroscopy in 2.1–2.3, a complete picture on the different crystallization processes during spin and slot-die coating can be derived.

3. Conclusion

In summary, we investigated in detail the crystallization processes taking place during the one-step solution processing of MAPbI_3 via spin and slot-die coating using multimodal optical in situ spectroscopy. We measured in parallel the time evolution of PL, light scattering and absorption and utilized PL and absorption to monitor the crystallization of MAPbI_3 , while by measuring the scattered light the crystallization process of the optically inactive solvent complex phase was accessed.

From the time evolution of PL peak position, integrated scattered light intensity, and the optical density at different photon energies, we identified the signatures of the different crystallization processes. We find that for both methods, a solvent-complex phase emerges, followed by perovskite crystallization. The latter occurs in two steps, separated in time for spin coating, while for slot-die coating only one perovskite crystallization phase could be observed.

Further analysis of the time evolution of the optical parameters and their derivatives allowed accessing the kinetics of each crystallization process. This in turn allowed investigating the behavior of the crystallization kinetics upon systematically altering the evaporation rate. Furthermore, the time duration of the complex phase formation was found to be a suitable independent parameter to identify differences in perovskite crystallization kinetics between slot-die and spin coating on a relative time scale. For both processing methods, the solvent-complex structure formation and the subsequent perovskite crystallization were independent of the evaporation rate on a relative time scale. In contrast, the second perovskite crystallization during spin coating proceeds restrictedly with a reduced perovskite crystal growth rate, where the average crystal sizes do not exceed $\approx 10 \text{ nm}$ in at least one spatial direction.

Here, the rapid decrease in solvent level at the beginning of spin coating, the spectral signature of the scattered light and microscopy images of the final film revealed that an increased polycrystallinity and flatter orientation of the solvent-complex phase are responsible for the changed perovskite crystallization kinetics.

On the one hand, our work demonstrates that multimodal optical in situ spectroscopy, combined with detailed data analysis represents a powerful tool to gain fundamental insights on the crystallization processes during solution-based halide perovskite processing. By identifying w_{complex} as a suitable independent parameter, we were able to compare the crystallization kinetics for both processing techniques quantitatively. Further, the methodology presented in this work yields potential to also achieve improved process and film control, e.g., in an industrial context. Here, monitoring (besides PL) the optical transmission signal that contains contributions from absorption as well as light scattering during the processing can give important information about the film coverage and film thickness, i.e., about the film quality. In the future, the presented methodology can be applied to state-of-the-art precursor chemistries or solvent mixtures relevant for industrially favorable one-step processing, and combining multimodal optical spectroscopy with, e.g., in situ X-ray scattering measurements would further allow to gain broader insights, e.g., about the perovskite phase purity.

On the other hand, our work also highlights the high sensitivity of perovskite crystallization kinetics on changes of the properties of the precursor phase from which perovskite forms. It thus represents an important step to enhance the general understanding of the crystallization processes occurring during halide perovskite evolution, independent of the specific solution-based coating method.

4. Experimental Section

Thin Film Fabrication: Precursors were used as received. Methylammonium iodide (MAI) was purchased from Dyesol and Lead(II) iodide (PbI_2 , 99%) was purchased from Acros. ITO substrates were cleaned in an ultrasonic bath with isopropanol (IPA, analytical grade (VWR)) followed by O_2 plasma treatment prior to use. For precursor solutions used for spin coating and for slot-die coating, MAI and PbI_2 were dissolved in DMF ($>99.5\%$, Fisher Chemical) with a concentration of 0.7 M .

Spin-coated perovskite films were prepared using a custom-built spin coater on ITO substrates with spin speeds of 500 to 2000 rpm in a one-step processing approach, using 70 μL of precursor solution per substrate at RT. The setup is shown in Figure S1a in the Supporting Information.

Slot-die coated perovskite films were prepared using an nRad slot-die coater system (nTact) on ITO substrates with a coating speed of 40 mm s^{-1} , a gap distance of 60 μm and a solvent dispensing rate of 100 $\mu\text{L s}^{-1}$ at RT. An air knife (Super Air Knife, Exair) was directed parallel to the printed precursor film with air pressure between 0.5 and 4 bar. The setup is shown in Figure S1b in the Supporting Information.

Spin coatings and slot-die coatings were performed at ambient air with a relative humidity in the range of 50%–60%.

In Situ Optical Spectroscopy: In situ optical spectra were recorded with the setup detailed in Section S1 in the Supporting Information. For the spin coating measurements, the scattered light of a LED emitting at 490 nm was measured, whereas for slot-die coating, the scattered room light was detected. PL and scattered light were measured simultaneously in one spectrum. PL/scattered light and absorption were then recorded alternating frame by frame, with a frame rate (for pairs of PL/scattered light and absorption) of 7.5 Hz in the case of slot-die coating and spin coating at 500 rpm, and with a frame rate of 11.6 Hz for spin coating with faster spin speeds (i.e., 600–2000 rpm).

Microscopy: Images of the solution processed films were taken with a Leica DM 2700M using Leica N Plan EPI objectives (20 \times /0.40 BD and 100 \times /0.85 BD).

Scanning Electron Microscopy: The samples were characterized by SEM using a Zeiss Ultra plus, equipped with a field-emission cathode using an in-lens secondary electron detector and an accelerating voltage of 3.0 kV.

Supporting Information

Supporting Information is available from the Wiley Online Library or from the author.

Acknowledgements

K.S. and C.G. contributed equally to this work. F.P. acknowledges funding from the German Academic Exchange Service (DAAD) in the framework of a Postdoc Research Grant (Postdoc-Program, Scholarship ID: 57407594). K.S. acknowledges financial support by the German National Science Foundation DFG via the project Ko 3973/2-1. C.G. and E.M.H. acknowledge financial support by the German National Science Foundation DFG through TUM International Graduate School of Science and Engineering (IGSSE). The Bavarian State Ministry of Science, Research, and the Arts is thanked for the support through the Collaborative Research Network “Solar Technologies go Hybrid.” Martina Heider and the KeyLab Electron and Optical Microscopy of the Bavarian Polymer Institute (BPI) are thanked for SEM images. Santosh Shanmugam is thanked for the help with the slot-die coating setup.

Correction added on 1 September 2021, after first online publication: Projekt Deal funding statement has been added.

Open access funding enabled and organized by Projekt DEAL.

Conflict of Interest

The authors declare no conflict of interest.

Data Availability Statement

Research data are not shared.

Keywords

absorption, halide perovskites, light scattering, photoluminescence, thin film formation

Received: June 8, 2021

Revised: July 13, 2021

Published online:

- [1] N. R. E. Laboratory Best Research-Cell Efficiency Chart, www.nrel.gov/pv/assets/pdfs/best-research-cell-efficiencies.20200104.pdf (accessed: April 2021).
- [2] M. M. Lee, J. Teuscher, T. Miyasaka, T. N. Murakami, H. J. Snaith, *Science* **2012**, 338, 643.
- [3] H.-S. Kim, C.-R. Lee, J.-H. Im, K.-B. Lee, T. Moehl, A. Marchioro, S.-J. Moon, R. Humphry-Baker, J.-H. Yum, J. E. Moser, M. Graetzel, N.-G. Park, *Sci. Rep.* **2012**, 2, 591.
- [4] A. Kojima, K. Teshima, Y. Shirai, T. Miyasaka, *J. Am. Chem. Sci.* **2009**, 131, 6050.
- [5] Y. Vaynzof, *Adv. Energy Mater.* **2020**, 10, 2003073.
- [6] Y. Zhong, R. Munir, J. Li, M.-C. Tang, M. R. Niazi, D.-M. Smilgies, K. Zhao, A. Amassian, *ACS Energy Lett.* **2018**, 3, 1078.
- [7] S. S. Shin, E. J. Yeom, W. S. Yang, S. Hur, M. G. Kim, J. Im, J. Seo, J. H. Noh, S. I. Seok, *Science* **2017**, 356, 167.
- [8] H. W. Ro, J. M. Downing, S. Engmann, A. A. Herzing, D. M. DeLongchamp, L. J. Richter, S. Mukherjee, H. Ade, M. Abdelsamie, L. K. Jagadamma, A. Amassian, Y. Liu, H. Yan, *Energy Environ. Sci.* **2016**, 9, 2835.
- [9] D.-Y. Son, J.-W. Lee, Y. J. Choi, I.-H. Jang, S. Lee, P. J. Yoo, H. Shin, N. Ahn, M. Choi, D. Kim, N.-G. Park, *Nat. Energy* **2016**, 1, 16081.
- [10] W. S. Yang, J. H. Noh, N. J. Jeon, Y. C. Kim, S. Ryu, J. Seo, S. I. Seok, *Science* **2015**, 348, 1234.
- [11] Y. Deng, E. Peng, Y. Shao, Z. Xiao, Q. Dong, J. Huang, *Energy Environ. Sci.* **2015**, 8, 1544.
- [12] Y. Tidhar, E. Edri, H. Weissman, D. Zohar, G. Hodes, D. Cahen, B. Rybtchinski, S. Kirmayer, *J. Am. Chem. Sci.* **2014**, 136, 13249.
- [13] P. W.-K. Fong, H. Hu, Z. Ren, K. Liu, L. Cui, T. Bi, Q. Liang, Z. Wu, J. Hao, G. Li, *Adv. Sci.* **2021**, 8, 2003359.
- [14] P. W.-K. Fong, G. Li, *Front. Mater.* **2021**, 8, 635224.
- [15] M. Kim, S.-Y. Ham, D. Cheng, T. A. Wynn, H. S. Jung, Y. S. Meng, *Adv. Energy Mater.* **2021**, 11, 2001753.
- [16] K. Meng, L. Wu, Z. Liu, X. Wang, Q. Xu, Y. Hu, S. He, X. Li, T. Li, G. Chen, *Adv. Mater.* **2018**, 30, 1706401.
- [17] Q. Hu, L. Zhao, J. Wu, K. Gao, D. Luo, Y. Jiang, Z. Zhang, C. Zhu, E. Schaible, A. Hexemer, *Nat. Commun.* **2017**, 8, 15688.
- [18] S. Lee, M.-C. Tang, R. Munir, D. Barrit, Y.-J. Kim, R. Kang, J.-M. Yun, D.-M. Smilgies, A. Amassian, D.-Y. Kim, *J. Mater. Chem. A* **2020**, 8, 7695.
- [19] L. E. Mundt, L. T. Schelhas, *Adv. Energy Mater.* **2020**, 10, 1903074.
- [20] O. Filonik, M. E. Thordardottir, J. Lebert, S. Pröller, S. Weiss, L. J. Haur, A. Priyadarshi, P. Fontaine, P. Mueller-Buschbaum, N. Mathews, E. M. Herzig, *Energy Technol.* **2019**, 7, 1900343.
- [21] D. Barrit, P. Cheng, M.-C. Tang, K. Wang, H. Dang, D.-M. Smilgies, S. (F.) Liu, T. D. Anthopoulos, K. Zhao, A. Amassian, *Adv. Funct. Mater.* **2019**, 29, 1807544.
- [22] K. S. Wilson, C. Y. Wong, *J. Phys. Chem. A* **2018**, 122, 6438.
- [23] Y.-M. Xie, B. Yu, C. Ma, X. Xu, Y. Cheng, S. Yuan, Z.-K. Wang, H. T. Chandran, C.-S. Lee, L.-S. Liao, S.-W. Tsang, *J. Mater. Chem. A* **2018**, 6, 9081.
- [24] K. Bruening, B. Dou, J. Simonaitis, Y.-Y. Lin, M. F. A. M. van Hest, C. J. Tassone, *Joule* **2018**, 2, 2464.
- [25] K. Schötz, F. Panzer, *J. Phys. Chem. A* **2021**, 125, 2209.
- [26] C. M. Sutter-Fella, *Adv. Energy Mater.* **2021**, 11, 2003534.

- [27] K. Suchan, J. Just, P. Becker, E. L. Unger, T. Unold, *J. Phys. Chem. A* **2020**, *8*, 10439.
- [28] S.-G. Kim, J.-H. Kim, P. Ramming, Y. Zhong, K. Schötz, S. J. Kwon, S. Hüttner, F. Panzer, N.-G. Park, *Nat. Commun.* **2021**, *12*, 1554.
- [29] M. Abdelsamie, T. Li, F. Babbe, J. Xu, Q. Han, V. Blum, C. M. Sutter-Fella, D. B. Mitzi, M. F. Toney, *ACS Appl. Mater. Interfaces* **2021**, *13*, 13212.
- [30] T.-B. Song, Z. Yuan, M. Mori, F. Motiwala, G. Segev, E. Masquelier, C. V. Stan, J. L. Slack, N. Tamura, C. M. Sutter-Fella, *Adv. Funct. Mater.* **2020**, *30*, 1908337.
- [31] M. Abdelsamie, J. Xu, K. Bruening, C. J. Tassone, H.-G. Steinrueck, M. F. Toney, *Adv. Funct. Mater.* **2020**, *30*, 2001752.
- [32] A. A. Petrov, I. P. Sokolova, N. A. Belich, G. S. Peters, P. V. Dorovatovskii, Y. V. Zubavichus, V. N. Khrustalev, A. V. Petrov, M. Graetzel, E. A. Goodilin, A. B. Tarasov, *J. Phys. Chem. C* **2017**, *121*, 20739.
- [33] A. D. Taylor, Q. Sun, K. P. Goetz, Q. An, T. Schramm, Y. Hofstetter, M. Litterst, F. Paulus, Y. Vaynzof, *Nat. Commun.* **2021**, *12*, 1878.
- [34] K. Liu, Q. Liang, M. Qin, D. Shen, H. Yin, Z. Ren, Y. Zhang, H. Zhang, P. W. K. Fong, Z. Wu, J. Huang, J. Hao, Z. Zheng, S. K. So, C.-S. Lee, X. Lu, G. Li, *Joule* **2020**, *4*, 2404.
- [35] W. Nie, H. Tsai, R. Asadpour, J.-C. Blancon, A. J. Neukirch, G. Gupta, J. J. Crochet, M. Chhowalla, S. Tretiak, M. A. Alam, H.-L. Wang, A. D. Mohite, *Science* **2015**, *347*, 522.
- [36] N. J. Jeon, J. H. Noh, Y. C. Kim, W. S. Yang, S. Ryu, S. I. Seok, *Nat. Mater.* **2014**, *13*, 897.
- [37] Y. Galagan, *Oxford Open Mater. Sci.* **2021**, *1*, itaa004.
- [38] M.-C. Tang, Y. Fan, D. Barrit, X. Chang, H. X. Dang, R. Li, K. Wang, D.-M. Smilgies, S. (F.) Liu, T. D. Anthopoulos, K. Zhao, A. Amassian, *J. Mater. Chem. A* **2020**, *8*, 1095.
- [39] M. Buchhorn, S. Wedler, F. Panzer, *J. Phys. Chem. A* **2018**, *122*, 9115.
- [40] M. Chauhan, Y. Zhong, K. Schötz, B. Tripathi, A. Köhler, S. Huettnner, F. Panzer, *J. Phys. Chem. A* **2020**, *8*, 5086.
- [41] H. E. W. Francis, A. Jenkins, *Fundamentals of Optics*, Tata McGraw-Hill Education, New York **1937**.
- [42] R. Munir, A. D. Sheikh, M. Abdelsamie, H. Hu, L. Yu, K. Zhao, T. Kim, O. E. Tall, R. Li, D.-M. Smilgies, *Adv. Mater.* **2017**, *29*, 1604113.
- [43] Y. Tian, I. G. Scheblykin, *J. Phys. Chem. Lett.* **2015**, *6*, 3455.
- [44] X. Zhu, H. Su, R. A. Marcus, M. E. Michel-Beyerle, *J. Phys. Chem. Lett.* **2014**, *5*, 3061.
- [45] T. W. Crothers, R. L. Milot, J. B. Patel, E. S. Parrott, J. Schlipf, P. Mueller-Buschbaum, M. B. Johnston, L. M. Herz, *Nano Lett.* **2017**, *17*, 5782.
- [46] M. Blencowe, *Designing Valve Preamps for Guitar and Bass, Second Edition*, Wern Publishing, **2013**.
- [47] S. Demchyshyn, J. M. Roemer, H. Groiß, H. Heilbrunner, C. Ulbricht, D. Apaydin, A. Böhm, U. Rütt, F. Bertram, G. Hesser, *Sci. Adv.* **2017**, *3*, e1700738.
- [48] L. Protesescu, S. Yakunin, M. I. Bodnarchuk, F. Krieg, R. Caputo, C. H. Hendon, R. X. Yang, A. Walsh, M. V. Kovalenko, *Nano Lett.* **2015**, *15*, 3692.
- [49] L. Wang, N. E. Williams, E. W. Malachosky, J. P. Otto, D. Hayes, R. E. Wood, P. Guyot-Sionnest, G. S. Engel, *ACS Nano* **2017**, *11*, 2689.
- [50] V. Malgras, J. Henzie, T. Takei, Y. Yamauchi, *Chem. Commun.* **2017**, *53*, 2359.
- [51] E. S. Parrott, J. B. Patel, A.-A. Haghighirad, H. J. Snaith, M. B. Johnston, L. M. Herz, *Nanoscale* **2019**, *11*, 14276.
- [52] Y. Kayanuma, *Phys. Rev. B* **1988**, *38*, 9797.
- [53] A. Buin, R. Comin, A. H. Ip, E. H. Sargent, *J. Phys. Chem. C* **2015**, *119*, 13965.
- [54] K. Schötz, A. M. Askar, W. Peng, D. Seeberger, T. P. Gujar, M. Thelakkat, A. Köhler, S. Huettnner, O. M. Bakr, K. Shankar, *J. Phys. Chem. C* **2020**, *8*, 2289.
- [55] P. Fassel, V. Lami, F. J. Berger, L. M. Falk, J. Zaumseil, B. S. Richards, I. A. Howard, Y. Vaynzof, U. W. Paetzold, *Matter* **2021**, *4*, 1391.
- [56] D. Hong, J. Li, S. Wan, I. G. Scheblykin, Y. Tian, *J. Phys. Chem. C* **2019**, *123*, 12521.
- [57] J. B. Patel, A. D. Wright, K. B. Lohmann, K. Peng, C. Q. Xia, J. M. Ball, N. K. Noel, T. W. Crothers, J. Wong-Leung, H. J. Snaith, *Adv. Energy Mater.* **2020**, *10*, 1903653.
- [58] M. Wang, K. Wang, Y. Gao, J. I. Khan, W. Yang, S. De Wolf, F. Laquai, *Sol. RRL* **2021**, *5*, 2100029.
- [59] Y. Li, Z. Zhao, F. Lin, X. Cao, X. Cui, J. Wei, *Small* **2017**, *13*, 1604125.
- [60] Y. Zhao, H. Tan, H. Yuan, Z. Yang, J. Z. Fan, J. Kim, O. Voznyy, X. Gong, L. N. Quan, C. S. Tan, *Nat. Commun.* **2018**, *9*, 1607.
- [61] Y.-H. Deng, Z.-Q. Yang, R.-M. Ma, *Nano Convergence* **2020**, *7*, 25.
- [62] J. Ding, S. Du, Y. Zhao, X. Zhang, Z. Zuo, H. Cui, X. Zhan, Y. Gu, H. Sun, *J. Mater. Sci.* **2017**, *52*, 276.